Airborne spectral measurements of surface–atmosphere anisotropy for arctic sea ice and tundra

G. Thomas Arnold

Emergent Information Technologies, Vienna, Virginia

Si-Chee Tsay,

NASA Goddard Space Flight Center, Greenbelt, Maryland

Michael D. King,

NASA Goddard Space Flight Center, Greenbelt, Maryland

Jason Y. Li,

Emergent Information Technologies, Vienna, Virginia

Peter F. Soulen

Joint Center for Earth Systems Technology, University of Maryland Baltimore County, Baltimore, Maryland

Short title: Airborne measurements of arctic surface anisotropy

International Journal of Remote Sensing

(Submitted November 1999; Revised January 2001)

G. Thomas Arnold
Emergent Information Technologies
2600 Park Tower Drive, Suite 1000 Vienna, Va
(301) 614-6229
(301) 614-6420 (fax)
tom.arnold@emergent-IT.com

Dr. Michael D. King
NASA Goddard Space Flight Center
Code 900
Greenbelt, MD 20771
(301) 614-5636

Jason Y. Li
Emergent Information Technologies
2600 Park Tower Drive, Suite 1000 Vienna, Va
(301) 614-6230

Dr. Peter F. Soulen
Joint Center for Earth Systems Technology
University of Maryland Baltimore County
Baltimore, Maryland

Dr. Si-Chee Tsay
NASA Goddard Space Flight Center
Code 913
Greenbelt, MD 20771
(301) 614-6188

Abstract

Angular distributions of spectral reflectance for four common arctic surfaces: snow-covered sea ice, melt-season sea ice, snow-covered tundra, and tundra shortly after snowmelt were measured using an aircraft based, high angular resolution (1-degree) multispectral radiometer. Results indicate bidirectional reflectance is higher for snow-covered sea ice than melt-season sea ice at all wavelengths between 0.47 and 2.3 μm, with the difference increasing with wavelength. Bidirectional reflectance of snow–covered tundra is higher than for snow-free tundra for measurements less than 1.64 μm, with the difference decreasing with wavelength. Bidirectional reflectance patterns of all measured surfaces show significant reflectance maxima in the forward scattering direction of the principal plane with identifiable specular reflection for the melt-season sea ice and snow-free tundra cases. The snow-free tundra had the most significant backscatter (similar to other vegetative bidirectional reflectance patterns such as for Cerrado in Brazil), and the melt-season sea ice the least. For sea ice, bidirectional reflectance changes due to snowmelt were more significant than differences among the different types of melt-season sea ice.

Also the spectral-hemispherical (plane) albedo of each measured arctic surface was computed. Comparing measured nadir reflectance to albedo for sea ice and snow-covered tundra shows nadir reflectance 5-40% smaller, with the largest difference at wavelengths beyond 1 μm. For snow-free tundra, nadir reflectance is 30-50% smaller than the plane albedo.

1. Introduction

The interaction of solar radiation with various arctic surfaces is an important component of the arctic climate. A measure of this interaction is the surface bidirectional reflectance function (BRF). Since most surfaces do not reflect uniformly in all directions, full description of the reflectance from a given surface requires knowledge of the full angular distribution of reflectance. Remote sensing instruments typically have narrow fields of view, and measure only the reflected radiance at a single angle (thus only a small portion of the full angular distribution). Even the next generation satellites (King 1999) will measure reflectance at a limited number of view angles. Thus proper interpretation of the remote sensing data will require knowledge of the full angular distribution of reflectance of all surface types.

The Cloud Absorption Radiometer (CAR) (King *et al.* 1986) flying aboard the University of Washington C-131A aircraft has provided a convenient and efficient means of obtaining BRF data. CAR BRF data over the past decade have been collected for several surface types. BRF data collected during the Kuwait Oil Fire Smoke Experiment (KOFSE) over an oil fire generated smoke layer is described by King (1992). Tsay *et al. (*1998) describe BRF data gathered in Brazil over cerrado, dense forest, and smoke over dense forest, during the Smoke Clouds and Radiation – Brazil experiment (SCAR-B). Additional BRF data for the Saudi Arabian desert, forested wet land (Great Dismal Swamp), and ocean water containing sunglint over the Atlantic Ocean and Persian Gulf have been discussed by Soulen *et al.* (1999). In this work we present BRF data of four common arctic surfaces: snow-covered sea ice, melt-season sea ice, snow-covered tundra, and tundra shortly after snowmelt. The snow-covered sea ice and tundra data were collected as part of the arctic Lead Experiment (LEADEX), and the

melt-season sea ice and tundra BRF data were collected during the Arctic Radiation Measurements in Column Atmosphere-Surface System (ARMCAS) experiment.

Several studies of sea ice reflective characteristics have been reported (Grenfell and Maykut 1977, Grenfell and Perovich 1984, Perovich *et al.* 1986, Allison *et al.* 1993, and DeAbreu *et al.* 1995). These sea ice studies, using typically ground-based instrumentation in mostly diffuse light conditions (overcast sky), discuss sea ice characteristics and their spatial and temporal effects on both spectral and wavelength-integrated albedo. Highlighted in particular are the changes that occur with the onset of the melt-season. Prior to the melt-season (usually about late May in the arctic), sea ice albedo is mostly a function of the optical properties of the "dry" snow cover that overlies the sea ice. With the onset of the melt-season, however, the snow cover quickly begins to melt. Sea ice albedo then becomes a function of the sea ice characteristics such as brine and bubble concentrations, ice temperature, and ice thickness, coupled with the local meteorology (freeze-thaw cycles). The result is increased spatial variability and reduced reflectivity at all wavelengths (especially above about 1 μm where nearly all the incident solar radiation is absorbed).

Direct application of these sea ice studies to remote sensing data (due to the characteristics of the remote sensing data) have heretofore been limited. To make the limited view angle remote sensing data more directly applicable, knowledge of the BRF at all azimuthal and polar viewing angles is needed. BRF of snow has been addressed in several studies (Dirmhirn and Eaton 1975, Kuhn 1985, Steffen 1987, Dozier *et al.* 1988, Hall *et al.* 1993, Warren *et al.* 1998 (includes a comprehensive review of factors affecting the BRDF of snow), and Aoki *et al.* 2000), but BRF of sea ice has been limited. Perovich (1991) found that at azimuth

angles 0˚ and 90˚ from solar incidence, reflectance of a refrozen melt pond and young sea ice 0.2 m thick was relatively constant for viewing zenith angles out to about 50˚, but increased sharply for larger zenith angles. Perovich (1994) reports that for sea ice progressing from cold dry snow-covered (pre-melt) conditions through various stages of melting, BRF data in the wavelength range 0.4 – 1.0 μm, at a viewing zenith angle of 30˚ is nearly azimuthally isotropic, but has a notable specular peak at a viewing zenith angle of 60˚ and azimuth of 0˚. Both of these studies, however, were limited in wavelength range and number of viewing zenith angles measured.

BRF studies of arctic tundra have also been limited. Recently, however, Vierling *et al.* (1997) and Eck *et al.* (1997) have reported results of ground-based BRF measurements taken during ARMCAS. They used the portable apparatus for rapid acquisition of bidirectional observations of the land and atmosphere (PARABOLA) to measure the BRDF of three types of arctic tundra: wet sedge (northernmost tundra), non-woody tussock tundra, and woody tussock tundra. The PARABOLA measures the nearly complete BRDF of three wavelength regions, but with an instantaneous field-of-view of 15°. Eck *et al.* (1997) report total albedo computed from the PARABOLA measurements to compare within 7.5% of pyranometer based measurements. Vierling *et al. (*1997) discuss how to use the BRDF measurements to differentiate between the three types of arctic tundra.

In this paper the BRF data for each arctic surface are also used to compute surface hemispherical albedo. Surface hemispherical albedo represents the "true" albedo for a given surface. However, nadir reflectance (often the parameter measured from an aircraft or satellite) is sometimes used as a surrogate (Barnsley *et al.* 1994). Perovich (1994) reports that for sea ice evolving through the different melting stages, the spectral shape of nadir reflectance for wave-

lengths from 0.4 to 1.0 μm is similar to the spectral albedo shape. The ratio of these two parameters was high (near 1.0) for the dry snow but, as melting progressed, the ratio decreased, especially at longer wavelengths. Similar comparisons have been done from our measurements and are described below.

In the next section, we quantitatively define surface bidirectional reflectance (as used in this work) and how hemispherical albedo is computed. In section 3, the instrumentation and data strategy are summarized, followed by discussion in section 4 of each measured surface spectral anisotropy and hemispherical albedo computation. A summary of this work is given in section 5.

2. Definitions

According to the National Bureau of Standards, the spectral bidirectional reflectance distribution function (Nicodemus *et al*. 1977), ρ_λ, is defined as

$$\rho_\lambda(\theta_r,\phi_r;\theta_i,\phi_i) = \frac{dI_\lambda(\theta_r,\phi_r;\theta_i,\phi_i)}{dF_\lambda(\theta_i,\phi_i)}, \tag{1}$$

which is a ratio of two derivatives; F_λ is the collimated irradiance illuminating at zenith angle θ_i and azimuth angle ϕ_i; and I_λ is the corresponding reflected radiance at angles θ_r and ϕ_r. In Eq. (1), ρ_λ is in units of sr^{-1}. However as detailed in Tsay *et al.* (1998), in dealing with actual measurements and applications, this definition is not practical. We instead (following Tsay *et al.* (1998)) characterize the surface anisotropy from spectral measurements following the definition of bidirectional reflection function (BRF, R_λ) found in van de Hulst (1980) and given by

$$R_\lambda(\theta,\theta_0,\phi) = \frac{\pi I_\lambda(\theta,\theta_0,\phi)}{\mu_0 F_\lambda}, \tag{2}$$

where θ and θ_0 are the viewing and illumination zenith angles respectively; ϕ is the azimuth angle between the viewing and illumination directions; $\mu_0 = \cos\theta_0$; F_λ

is the collimated irradiance; and I_λ is the corresponding reflected radiance. The collimated irradiance F_λ is computed by weighting the solar flux at the top of the atmosphere (TOA) with the spectral response function of each band, taking into account the eccentricity of the earth's orbit around the sun. For this definition downward TOA flux is used because the downward flux at the aircraft level was not fully measured (see Tsay *et al.* (1998) for greater details.)

Similarly for the spectral albedo, r_λ, radiance received by the detector from all viewing directions/solid angles are integrated (summed up for all IFOVs). Using Eq. (2), the spectral albedo is given by

$$\begin{aligned} r_\lambda(\theta_0) &= \frac{1}{\pi}\int_0^{2\pi}\int_0^{\pi/2} R_\lambda(\theta,\theta_0,\phi)\cos\theta\,\sin\theta\,d\theta\,d\phi, \\ &\cong \frac{1}{\mu_0 F_\lambda}\left[\sum_{i=1}^{M}\sum_{j=1}^{N} I_\lambda(\theta_i,\theta_0,\phi_j)\cos\theta_i\,\sin\theta_i\,\Delta\theta_i\,\Delta\phi_j\right], \end{aligned} \tag{3}$$

where (i, j) are the indices of (θ, ϕ) for discretization (M, N terms) respectively, over the hemisphere.

3. Instrumentation and data collection

During LEADEX and ARMCAS, measurements of surface-atmosphere bidirectional reflectance were acquired by using a multispectral scanning radiometer - the Cloud Absorption Radiometer (CAR), which was designed and built at NASA Goddard Space Flight Center (cf. King *et al*. (1986) for details). The CAR was mounted in the nose of the University of Washington's C-131A research aircraft, providing radiometric measurements at 13 discrete wavelengths between 0.3 and 2.3 μm. The first 7 channels are continuously recorded, whereas channels 8 through 13 are located in a filter-wheel that can be locked at a particular channel or manually or automatically rotated to measure a new wavelength interval after a preset number of scans. The wavelength location of each channel was se-

lected to minimize atmospheric absorption effects (except for the UV-B channel where it is desired). The visible channel reflectance is weakly reduced by ozone absorption, as well as by aerosol and Rayleigh scattering. Aerosol effects should be small due to the relatively clean arctic air for the ARMCAS measurements, though may be more significant for the LEADEX measurements (due to arctic haze commonly observed at that time of year). The shortwave-infrared channel reflectance can be reduced by 2-8% due to water vapor and trace gas absorption.

Viewing with an IFOV of 1°, the CAR scans in a vertical plane on the right hand side of the aircraft from 5° before zenith to 5° past nadir (190° aperture), thereby permitting observations of both zenith and nadir radiances to be obtained with as much as a 5° aircraft roll, an angle that is measured simultaneously with a gyroscope aboard the aircraft. Table 1 summarizes the CAR specifications.

The C-131A flew at an average speed of about 80 m s^{-1} in a circle with a minimum diameter of about 3 km, at a comfortable roll angle of 20° in about two minutes. At an altitude of 600 m above the targeted surface area and 1° IFOV, the pixel resolution is about 10 m at nadir and about 270 m at an 80° viewing angle from the CAR (see King (1992) and Tsay *et al.* (1998) for additional details).

4. Results from observations

The assumption of homogeneity of the targeted surface area is fundamental to properly reconstructing the bidirectional reflectance from CAR measurements. Thus targets were carefully selected to be as homogeneous as possible. During ARMCAS and LEADEX, eight spectral BRF data sets were obtained and analyzed. The location of each BRF study on the north slope of Alaska and nearby Arctic Ocean is shown in figure 1, which further designates the precise location

by assigning a letter from A-H. These eight studies have been categorized according to one of four types of surfaces measured: (i) snow-covered sea ice, (ii) melt-season sea ice, (iii) snow-covered tundra, or (iv) snow-free tundra. Two snow-covered sea ice BRF studies (A and B in figure 1) were acquired over the Beaufort Sea under nearly clear-sky conditions, from 20:50 to 20:57 and 21:15 to 21:24 UTC on April 7, 1992. Three melt-season sea ice BRFs (C, D, and E) were also acquired over the Beaufort Sea under nearly clear-sky conditions, from 00:44 to 00:55 UTC on June 6, 1995, and from 18:34 to 19:39 and 20:58 to 21:19 UTC on June 8, 1995. One snow-covered tundra BRF (F) was acquired just south of Prudhoe Bay, with nearly clear sky above (only some patchy thin cirrus), from 23:38 to 23:43 UTC on April 7, 1992. Finally, two snow-free tundra cases (G and H) were acquired south of Prudhoe Bay, with nearly clear sky above, from 06:37 to 06:48 and from 06:57 to 07:09 UTC on June 12, 1995.

4.1 Snow-covered sea ice (April 1995)

Two three-orbit BRFs under clear sky conditions were conducted over snow-covered multi-year sea ice (locations A and B in figure 1). The solar zenith angle θ_0 for the two cases varied from 65.14°-65.26° and 65.22°-65.35°, respectively (cf. table 2). Figure 2a shows a representative photograph of snow-covered sea ice taken in the area where these BRF measurements were obtained. Due to the optically thick snow cover (5-10 cm layer is optically thick (Grenfell and Maykut 1977)), the optical effects of the underlying sea ice are limited. Variations in surface reflectance are primarily due to shadowing caused by the relatively low sun angle and irregularities in the surface (pressure ridges). These effects are relatively small. The CAR filter-wheel channel was locked at 1.64 μm for 1 orbit in BRF A and for one orbit in B at 2.20 μm.

Figure 3 contains the spectral BRF for each measured CAR channel over the

snow-covered sea ice (since the BRF plots for A and B were similar, only those from A are shown here except for the 2.2 μm plot). In these and all other polar plots, zenith angle is represented as radial distance from the center, and azimuth angle as length of the arc on the respective zenith circle. The principal plane resides in the 0°-180° azimuthal plane with the sun located in the 0° azimuth direction. With this definition, the upper half circle represents forward scattering and the lower half represents backscattering, with the anti-solar direction at $\theta_0 \approx 65°$, denoted by the white spot in the upper left plot of figure 3a.

The BRF pattern in figure 3 shows reflectance minimized in the region around nadir and increasing going out from nadir, particularly in the solar and anti-solar directions. The strongest peak is in the forward scattering direction, while there is a diffuse and weaker peak in the backscattering direction. Interestingly, while the plot suggests a high degree of symmetry, reflectance mid-way between the solar and anti-solar directions is notably lower on the right than on the left in the dataset. The cause of this asymmetry is not clear, but one possible explanation is oriented sastrugi (Warren *et al.* 1998).

To investigate further the detailed angular distribution of BRF, figure 4a shows the spectral dependence of the reflection function along the principal plane. Except for the forward and backscattering regions near the limb, the plots for each band are otherwise fairly flat, representing a nearly Lambertian reflectance of snow-covered sea ice away from the specular reflectance direction.

4.2 Melt-season sea ice (June 1995)

The three melt-season sea ice cases were obtained in different geographical regions (locations C, D, and E in figure 1) to compare different types of sea ice. BRF C was 4 orbits, D was 35 orbits, and E was 10 orbits. Solar zenith angles varied from 54.51°-55.26°, 53.28°-57.69°, and 48.93°-49.45° respectively, for C, D,

and E. The filter-wheel was locked at 1.64 μm for 2, 13, and 4 orbits respectively, for C, D and E, and at 2.2 μm for 1, 9, and 4 orbits. A photo of the melt-season sea ice (from June 8) is shown in figure 2b. The BRF from C and E were both of younger shorefast ice but from different parts of the coastline. According to flight notes, the surface in E showed no evidence of open leads or melt ponds (although a few of what appear to be small islands were noted). Much of the variability of the surface is likely due to melting and re-freezing and varying thickness of the ice. As compared to snow-covered sea ice, surface characteristics of melt-season sea ice show much more variability, particularly at shorter wavelengths.

Data for BRFs C, D, and E are listed in table 2, and the BRF plot from D is presented in figure 5 (C and E are not shown but show similar features). The melt-season BRFs, like the snow-covered sea ice BRFs, show pronounced maxima in the forward scattering direction, and secondary maxima in the backscattering direction (though less apparent than for the snow-covered sea ice cases). Unlike the snow-covered sea ice, however, they show a distinct specular reflectance (sunglint) just to the right of the solar principal plane, and at an angle from nadir equivalent to the solar zenith angle (the small azimuth offset from the principal plane is an artifact resulting from the fixed mount of the CAR and the slight upward aircraft pitch). The most important difference though is that the reflectance values of all the CAR bands for the melt-season cases are lower than for the snow-covered sea ice[1]. This is most pronounced for the 1.6 and 2.1 μm channels (and in agreement with Grenfell and Perovich (1984)). The melt-season sea ice

[1] The albedo values of the 0.50 μm snow covered sea ice data and 0.47 μm melt-season sea ice data as shown in table 2 are similar. However the albedo of the snow-covered sea ice (relative to the melt-season sea ice) are suppressed by the larger solar zenith angle (increased Rayleigh scattering), and the slightly the longer wavelength

surface for these channels is absorbing nearly all of the incident sunlight. The principal plane plots in figure 4b show reflectance of 1-2% in these bands, considerably lower than the snow-covered sea ice in figure 4a.

4.3 Snow-covered tundra (April 1992)

Following the two snow-covered sea ice BRFs (locations A and B), the C-131A flew a two-orbit BRF pattern over snow-covered tundra to the south of Prudhoe Bay (F in figure 1). The solar zenith angle varied from 65.14°-65.35° (table 2), and the filter-wheel was locked at 1.64 μm for one orbit. A photo of snow-covered tundra is shown in figure 2c, with the Trans-Alaska Pipeline clearly evident in this photo. Figure 6 illustrates the two-orbit average BRF for this case, which again shows maximum reflectance in the forward scattering direction with some evidence for a secondary backscattering maximum, though less apparent than for snow-covered sea ice. The cause of the asymmetry, the minima in reflectance on the left-hand side of the circle is not clear, though (as for the snow-covered sea ice) orientated sastrugi could produce this effect. Reflectance values are generally slightly less than the snow-covered sea ice cases on this day, but are still quite high, even at 1.6 μm. A plot of the principal plane data is given in figure 7a. Snow covered tundra is quite Lambertian except for the forward scattering direction. This agrees well with measurements by Aoki *et al.* (2000) made over a flat snow surface. Using plots similar to figure 6 (except normalized by the reflectance at nadir), they show data away from the forward scattering direction to be fairly uniform (data values approximately 1.0) but increasing (greater than 1.0) towards forward scattering direction. Notable also is increase in magnitude of the data in the forward scattering direction with wavelength. Data for figure 6, normalized by the value at nadir (not shown here), show similar effects.

4.4 Snow-free tundra (June 1995)

Two BRF studies (5 orbits each) were conducted over the tundra south of Prudhoe Bay on June 12, 1995 (G and H in figure 1). These were "midnight sun" flights (solar zenith varied from 80.63°-81.23° and 82.00°-82.61°, respectively). The filter-wheel was locked at 1.64 μm for 3 and 2 orbits, respectively, for G and H and for 1 and 2 orbits, respectively, for 2.1 μm. The tundra vegetation common to this part of the north slope is senescent wet sedge (little photosynthesis since snow cover has just melted (Vierling *et al.* 1997)). Figure 1d shows a close-up photograph of this type of tundra surface. Though not apparent in this photograph, the wet sedge was in many places partially submerged. The BRF plot in figure 8 (from G) depicts a fairly symmetric reflectance pattern for each case, with a fairly narrow maximum in the forward scattering direction (probably specular reflection due to the water in the tundra) and a broader (and higher for bands 0.87 μm and longer) backscattering pattern. This BRF pattern is similar in shape to both the Brazilian cerrado (savannah) case described by Tsay *et al. (*1998) and the Great Dismal Swamp case described by Soulen *et al. (*1999), though with a much lower sun angle here. Each have a relatively flat reflectance pattern except for the maxima as you approach the horizon in the forward scattering direction of the principal plane and (for wavelengths of 0.87 μm and longer) the opposition point ("hot spot") in the backscattering direction. This pattern for the snow-free tundra is quite evident in the principal plane plot (for G) as shown in figure 7b.

4.5 Spectral Albedo

The spectral BRF measurements obtained by the CAR contain very fine angular resolution (i.e., $M = 90$ samples in θ and $N \approx 200$ in ϕ, *cf.* table 1) which produces virtually no computational error in discretizing the integral. By using Eq.

(3), it is straightforward to compute the spectral-hemispherical albedo (defined here as the ratio of the upward flux and the downward flux at TOA) for the sea ice and tundra surfaces. The results for each of the sea ice and tundra cases are listed in tables 2 and 3, respectively. For each BRF case, columns 1 and 2 in each table lists the central wavelength and bandwidth characteristics of each CAR channel (note the change in channel 1 between 1992 and 1995). Column 3 lists the corresponding solar flux computed by weighting the solar flux at the top of the atmosphere with the spectral response function of each channel. The solar fluxes vary slightly from case to case due to the eccentricity of the earth's orbit about the sun. In column 4, the solar zenith angle varies less than 2° for all but one BRF case (the 35 circle average of location D ~ 4.4°). Thus change in solar zenith angle does not contribute significantly to the variation in the computed spectral albedo (column 5). This variation is due largely to surface inhomogeneity. Column 6 lists the average reflectance value and variation at nadir for each BRF study, for comparison to the spectral albedo.

Generally for sea ice cases, the spectral albedo values in table 2 are consistent within a season, but show important differences when comparing the snow-covered sea ice to the melt-season sea ice, particularly for the longer wavelengths. The difference at the shortest wavelengths are relatively small[2], about 10% at 0.67 μm, increasing substantially with wavelength to about a factor of 2 at 1.03 μm, to a factor of 6 or more at 1.64 μ*m*. Also shown in table 2, the greater variability of the melt-season sea ice albedo at the shortest wavelength is indicative of a more variable surface (open leads, melt ponds, various types of bare ice, etc.) at this time of year.

---

[2] Quantitative comparison at the shortest wavelengths is more significantly affected by atmospheric effects (particularly Rayleigh scattering) than the longer wavelengths.

Nadir reflectance values as a function of wavelength are also presented in table 2 for each of the sea ice cases. Similar to the conclusion of Perovich (1994), the trends of hemispherical albedo and nadir reflectance as a function of wavelength are similar (if plotted would have nearly the same spectral shape). Furthermore comparing the albedo of sea ice to the nadir reflectance (figure 9), often used as a surrogate for surface albedo in climate models yields two conclusions. First, at essentially all CAR wavelengths, the nadir snow-covered sea ice reflectance is a better surrogate for albedo than the melt-season sea ice albedo. Second, for both sea ice types, differences between hemispherical albedo and nadir reflectance exceed 10% only for CAR wavelengths greater than about 1 μm (differences can be as much as 45%).

Table 3 lists the spectral albedo and nadir reflectance values for the tundra cases. The snow-covered tundra albedos are slightly smaller than the snow-covered sea ice albedos at all wavelengths (cf. table 2). Possible causes of this bias include age differences of the snow, temperature differences (degree of wetness of snow), contamination, and the effects due to underlying differences in surface reflectance (function of snow depth). Grenfell and Perovich (1984) discuss these types of effects in further detail. Since no samples were collected of the snow in either case, it is not possible to determine the relative role of each of these effects. The difference in snow-covered tundra albedo as compared to snow-free tundra, however, is much more apparent. The snow-covered tundra albedo values are much higher than the snow-free tundra albedos at all visible wavelengths, but this difference decreases with increasing wavelength, and actually reverses at 1.64 μm (cf. table 2). Noteworthy also for the snow free tundra are much higher albedos (and nadir reflectance) for wavelengths 0.87 μm and longer, as compared to the 0.47 and 0.68 μm values. This is consistent with the

property of vegetation having a significant increase in reflectance for wavelengths greater than about 0.7 μm (Gates 1980).

Comparison of the hemispheric albedo of the snow-covered tundra to the measured nadir reflectance, similar to the sea ice cases, indicates only a small underestimate of the true albedo for wavelengths less than about 1 μm. Differences can be as much as 40% for observations above 1 μm. For the snow-free tundra, however, the underestimate is much greater (cf. figure 9). The underestimate ranges from about 30-50% and, unlike sea ice, the largest differences occur at the shortest wavelengths.

5. Summary

An important part of a successful effort to monitor the Earth's climate in the EOS era is the proper treatment of the sun's interaction with each type of Earth surface. To accurately interpret satellite measurements of top-of-the-atmosphere radiance, it is necessary to know the bidirectional reflectance function of each Earth surface. Thus the radiative effects of natural surfaces should be taken into account for remote sensing of aerosols and clouds, and also accurate surface hemispherical albedos can be determined for input to global climate models.

During the LEADEX and ARMCAS field experiments, surface spectral bidirectional reflectance of sea ice and tundra for both snow-covered (pre-melt) and melt conditions were measured using the Cloud Absorption Radiometer (CAR). Snow-covered conditions for sea ice and tundra were measured on April 7, 1992. Sea ice in melt conditions was measured on June 5 and 8, 1995, and snow free tundra on June 12, 1995. Despite contamination of the CAR data due to Rayleigh scattering and minor gaseous absorption (aerosol scattering was assumed to be small), results show distinct spectral characteristics for all types of surfaces presented here, particularly the seasonal bidirectional reflectance changes in sea ice

and tundra surfaces. In all cases sea ice reflectivity decreases with the onset of the melt-season, with the degree of difference increasing with wavelength. Reflectivity of snow-covered tundra also decreased following snow-cover melt for CAR channels below 1.64 μm, but actually increased by a factor of two at 1.64 μm. In addition, detailed measurements of the angular distribution of spectral reflectance were used to compute hemispherical albedos for each surface. For sea ice and snow-covered tundra, the CAR data indicate the surface spectral anisotropy only becomes significant at wavelengths greater than about 1 μm. Snow-free tundra, on the other hand, exhibits large surface spectral anisotropy at all wavelengths, with the greatest anisotropy at the shortest CAR wavelengths (~0.47 μm). Underestimates of the true albedo ranged from 30-50% when using nadir reflectance as a proxy for hemispherical albedo.

The CAR measurements, combined with boundary layer aircraft measurements of aerosol physical properties and other co-located observations, form an unprecedented data set that is expected to greatly facilitate developing more realistic radiative transfer models in the future. All CAR data from both the ARMCAS and LEADEX field experiments have been processed to level-1b (calibrated and geolocated radiance). Information on where and how to obtain CAR data from these and other field experiments (including all BRF polar plots), as well as browse images, a CAR data user's guide, and software for unpacking and interpreting CAR data, may be found on the World Wide Web at ltpwww.gsfc.nasa.gov/CAR.

Acknowledgments. The authors are especially grateful to Prof. P. V. Hobbs and University of Washington personnel for helping to make these complex field projects and data collection a success. Thanks are also extended to Prof. S. G. Warren for his assistance in revising the manuscript. This research was sup-

ported by funding provided by the MODIS Science Team and NASA's Radiation Science Program. The University of Washington research flights during LEADEX were supported by the National Science Foundation under Grant DPP-9116371.

References

Allison, I., Brandt, R. E., and Warren, S. G., 1993, East Antarctic sea ice: albedo, thickness distribution, and snow cover, *J. Geophys. Res.,* **98**, 12417-12429.

Aoki, T., Aoki, A., Fukabori, M., Hachikubo, A., Tachibana, Y., and Nishio, F., 2000, Effects of snow physical parameters on spectral albedo and bidirectional reflectance of snow surface, *J. Geophys. Res.,* **105**, 10219-10236.

Barnsley, M. J., Strahler, A. H., Morris, K. P., and Muller J. P., 1994, Sampling the surface bidirectional reflectance distribution function (BRDF): 1. Evaluation of current and future satellite sensors, *Remote Sens. Rev.,* **8**, 271-311.

DeAbreu, R. A., Barber, D. G., Misurak, K., and LeDrew, E. F., 1995, Spectral albedo of snow-covered first-year and multi-year sea ice during spring melt, *Ann. Glaciol.,* **21**, 337-342.

Dirmhirn, I., and Eaton, F. D., 1975, Some characteristics of the albedo of snow, *J. Appl. Meteorol.,* **14,** 375-379.

Dozier, J., Davis, R. E., Chang, A. T., and Brown, K., 1988, The spectral bidirectional reflectance of snow, Proceedings of the 4th International Colloqium on Spectral Signatures of Objects in Remote Sensing, *Eur. Space Agency Spec. Publ.,* **ESA SP-287**, 87-92.

Eck, T. F., Deering, D. W., and Vierling, L. A., 1997, Arctic tundra albedo and its estimation from spectral hemispheric reflectance, *Int. J. Remote Sens.,* **18**, 3535-3549.

Gates, D. M., 1980, Spectral characteristics of radiation and matter. In Biophysical Ecology, (*Springer Verlag),* pp. 215-247

Grenfell, T. C., and Maykut, G. A., 1977, The optical properties of ice and snow in the Arctic Basin, *J. Glaciol.,* **18**, 445-463.

Grenfell, T. C., and Perovich, D. K., 1984, Spectral albedo of sea ice and incident

solar irradiance in the southern Beaufort Sea, *J. Geophys. Res.,* **89**, 3573-3580.

Grenfell, T. C., Warren, S. G., and Mullen, P.C., 1994, Reflection of solar radiation by the Antarctic snow surface at ultraviolet, visible and near-infrared wavelengths, *J. Geophys. Res.,* **99**, 18669-18684.

Hall, D. K., Foster, J. L., Irons, J. R., and Dabney, P. W., 1993, Airborne bidirectional radiances of snow-covered surfaces in Montana, U.S.A., *Ann. Glaciol,* **17**, 35-40.

King, M. D., Strange, M. G., Leone P., and Blaine, L. R., 1986, Multiwavelength scanning radiometer for airborne measurements of scattered radiation within clouds, *J. Atmos. Oceanic Tech.,* **3**, 513-522.

King, M. D., Ed., 1999, EOS Science Plan: The State of Science in the EOS Program, *NASA Report* **NP-1998-12-069-GSFC**, Goddard Space Flight Center, Greenbelt, MD, 397 pp.

King, M. D., 1992, Directional and spectral reflectance of the Kuwait Oil-Fire smoke, *J. Geophys. Res.,* **97**, 14545-14549.

Kuhn, M., 1985, Bidirectional reflectance of polar and alpine snow surfaces, *Ann. Glaciol.,* **6**, 2164-2167.

Nicodemus, F. E., Richmond, J. C., Hsia, J. J., Ginsberg, I. W., and Limperis, T., 1997, Geometrical considerations and nomenclature for reflectance, *Natl. Bur. Stand. Monogr., 160*, U.S. Govt. Print. Off., Washington, D. C., 52 pp.

Perovich, D. K., Maykut, G. A., and Grenfell, T. C., 1986, Optical properties of ice and snow in the polar oceans. I: observations, Ocean Optics 8, *Proc. SPIE Int. Soc. Opt. Eng.,* **637**, 232-241.

Perovich, D. K., 1991, Seasonal changes in sea ice optical properties during fall freeze-up, *Cold Reg. Sci. Technol.,* **19**, 261-273.

Perovich, D. K., 1994, Light reflection from sea ice during the onset of melt, *J.*

Geophys. Res., **99**, 3351-3359.

Soulen, P. F., King, M. D., Tsay, S., Arnold, G. T., and Li, J. Y., Airborne spectral measurements of surface anisotropy during SCAR-A, Kuwait oil-fire, and TARFOX experiments, *J. Geophys. Res.* **108**, 10203-10218.

Stefan, K., 1987,Bidirectional reflectance of snow at 500-600 nm, in large scale effects of seasonal snowcover, *IAHS Publ.,* **166,** 415-425.

Tsay, S. C., King, M. D., Arnold, G. T., and Li, J. Y., 1998, Airborne spectral measurements of surface anisotropy during SCAR-B, *J. Geophys. Res.,* **103**, 31943-31953.

van de Hulst, H. C., 1980, *Multiple Light Scattering: Tables, Formulas, and Applications*, 739 pp., Academic Press.

Vierling, L. A., Deering, D. W., and Eck, T. F., 1997, Differences in arctic tundra vegetation type and phenology as seen using bidirectional radiometry in the early growing season, *Remote Sens. Environ.,* **60**, 71-82.

Warren, S. G., Brandt, R. E., and Hinton, P. O., 1998, Effect of surface roughness on bidirectional reflectance of Antarctic snow, *J. Geophys. Res.,* **103**, 25789-25807.

Table 1. Cloud Absorption Radiometer specifications during field campaigns.

Platform	University of Washington C-131A aircraft
Ground speed	80 m s^{-1} (nominal)
Total field of view	190°
Instantaneous field of view	17.5 mrad (1°)
Pixels per scan line	395
Scan rate	100 scan lines per minute
Spectral channels	13 (7 continuously sampled and 6 in filter wheel)
Spectral range	0.472 (0.503) - 2.303 μm
Data system	8 channels @ 10 bits
Calibration	Integrating sphere on the ground

Table 2. Computed spectral albedo and measured nadir reflectance for snow-covered sea ice (A-B) and melt-season sea ice (C-E). Uncertainties do not include possible errors in calibration.

Central wave-length (μm)	Bandwidth (μm)	Solar flux (W m^{-2} μm^{-1})	Solar zenith angle	Albedo*	Nadir reflectance
(A) Snow-covered sea ice (April 7, 1992)					
0.503	0.016	1901.7	65.14° - 65.26°	0.737 ± 0.0040	0.680 ± 0.0262
0.673	0.020	1523.5	65.14° - 65.26°	0.770 ± 0.0034	0.718 ± 0.0292
0.754	0.019	1281.1	65.14° - 65.26°	0.818 ± 0.0029	0.776 ± 0.0315
0.866	0.020	947.85	65.14° - 65.26°	0.782 ± 0.0012	0.720 ± 0.0286
1.031	0.020	706.75	65.14° - 65.26°	0.710 ± 0.0036	0.627 ± 0.0264
1.220	0.021	497.66	65.14° - 65.26°	0.506 ± 0.0060	0.422 ± 0.0221
1.270	0.020	410.52	65.14° - 65.26°	0.408 ± 0.0058	0.343 ± 0.0187
1.640	0.041	232.27	65.20° - 65.26°	0.196	0.134 ± 0.0144
(B) Snow-covered sea ice (April 7, 1992)					
0.503	0.016	1901.7	65.22° - 65.35°	0.739 ± 0.0010	0.686 ± 0.0127
0.673	0.020	1523.5	65.22° - 65.35°	0.774 ± 0.0016	0.728 ± 0.0164
0.754	0.019	1281.1	65.22° - 65.35°	0.823 ± 0.0020	0.788 ± 0.0176
0.866	0.020	947.85	65.22° - 65.35°	0.784 ± 0.0013	0.730 ± 0.0168
1.031	0.020	706.75	65.22° - 65.35°	0.704 ± 0.0029	0.630 ± 0.0186
1.220	0.021	497.66	65.22° - 65.35°	0.496 ± 0.0059	0.421 ± 0.0196
1.270	0.020	410.52	65.22° - 65.35°	0.399 ± 0.0056	0.342 ± 0.0166
2.200	0.040	82.693	65.22° - 65.27°	0.199	0.137 ± 0.0132
(C) Melt-season sea ice (June 5, 1995)					
0.472	0.021	1962.9	54.51° - 55.26°	0.737 ± 0.0061	0.696 ± 0.0813
0.675	0.020	1471.7	54.51° - 55.26°	0.666 ± 0.0023	0.626 ± 0.0852
0.869	0.022	943.60	54.51° - 55.26°	0.581 ± 0.0024	0.519 ± 0.0772
1.038	0.020	671.13	54.51° - 55.26°	0.379 ± 0.0023	0.298 ± 0.0427
1.219	0.020	475.07	54.51° - 55.26°	0.189 ± 0.0025	0.130 ± 0.0194
1.271	0.021	430.81	54.51° - 55.26°	0.175 ± 0.0021	0.119 ± 0.0188
1.643	0.041	229.64	54.86° - 55.26°	0.032 ± 0.0022	0.019 ± 0.0085
2.207	0.040	72.250	54.51° - 54.69°	0.034	0.020 ± 0.0132
(D) Melt-season sea ice (June 8, 1995)					
0.472	0.021	1961.8	53.28° - 57.69°	0.734 ± 0.0191	0.689 ± 0.1367
0.675	0.020	1471.0	53.28° - 57.69°	0.640 ± 0.0192	0.592 ± 0.1293
0.869	0.022	943.11	53.28° - 57.69°	0.538 ± 0.0178	0.470 ± 0.1157
1.038	0.020	670.79	53.28° - 57.69°	0.341 ± 0.0128	0.265 ± 0.0684
1.219	0.021	474.83	53.28° - 57.69°	0.170 ± 0.0097	0.117 ± 0.0305
1.271	0.020	430.58	53.28° - 57.69°	0.156 ± 0.0092	0.105 ± 0.0274
1.643	0.041	229.52	55.19° - 57.69°	0.031 ± 0.0020	0.016 ± 0.0089
2.207	0.040	72.210	54.41° - 56.72°	0.031 ± 0.0024	0.019 ± 0.0128
(E) Melt-season sea ice (June 8, 1995)					
0.472	0.021	1961.8	48.93° - 49.45°	0.707 ± 0.0080	0.679 ± 0. 0996
0.675	0.020	1471.0	48.93° - 49.45°	0.619 ± 0.0110	0.592 ± 0.1100
0.869	0.022	943.11	48.93° - 49.45°	0.511 ± 0.0105	0.465 ± 0.1117
1.038	0.020	670.79	48.93° - 49.45°	0.319 ± 0.0068	0.259 ± 0.0615
1.219	0.021	474.83	48.93° - 49.45°	0.154 ± 0.0039	0.109 ± 0.0251
1.271	0.020	430.58	48.93° - 49.45°	0.145 ± 0.0040	0.101 ± 0.0232
1.643	0.041	229.52	49.22° - 49.45°	0.028 ± 0.0025	0.016 ± 0.0075
2.207	0.040	72.210	48.97° - 49.12°	0.025 ± 0.0013	0.017 ± 0.0111

* Albedo is defined in section 2 (eqn. 3) as the ratio of the ratio of the upward flux to the downward flux at the top of the atmosphere. The Albedo values at 0.47 and 0.50 μm and to a lesser extent, the 0.67 μm are significantly reduced by Rayleigh scattering.

Table 3. Computed spectral albedo and measured nadir reflectance for snow-covered tundra (F) and snow-free tundra (G, H). Uncertainties do not include possible errors in calibration.

Central wave-length (μm)	Bandwidth (μm)	Solar flux (W m^{-2} μm^{-1})	Solar zenith angle	Albedo	Nadir reflectance
(F) Snow-covered tundra (April 7, 1992)					
0.503	0.016	1901.7	65.14° - 65.35°	0. 698 ± 0.0141	0.663 ± 0.0253
0.673	0.020	1523.5	65.14° - 65.35°	0.725 ± 0.0189	0.698 ± 0.0338
0.754	0.019	1281.1	65.14° - 65.35°	0.770 ± 0.0214	0.755 ± 0.0376
0.866	0.020	947.85	65.14° - 65.35°	0.732 ± 0.0218	0.699 ± 0.0395
1.031	0.020	706.75	65.14° - 65.35°	0.659 ± 0.0221	0.606 ± 0.0403
1.220	0.021	497.66	65.14° - 65.35°	0.462 ± 0.0181	0.402 ± 0.0295
1.270	0.020	410.52	65.14° - 65.35°	0.379 ± 0.0146	0.330 ± 0.0256
1.640	0.040	232.27	65.14° - 65.24°	0.156	0.104 ± 0.0126
(G) Tundra – no snow (June 12, 1995)					
0.472	0.021	1962.9	80.63° - 81.23°	0.053 ± 0.0006	0.027 ± 0.0070
0.675	0.020	1471.7	80.63° - 81.23°	0.105 ± 0.0017	0.060 ± 0.0117
0.869	0.020	943.60	80.63° - 81.23°	0.266 ± 0.0041	0.174 ± 0.0249
1.038	0.020	671.13	80.63° - 81.23°	0.345 ± 0.0054	0.228 ± 0.0343
1.219	0.021	475.07	80.63° - 81.23°	0.318 ± 0.0047	0.214 ± 0.0335
1.271	0.020	430.81	80.63° - 81.23°	0.271 ± 0.0038	0.187 ± 0.0301
1.643	0.041	229.64	80.63° - 80.98°	0.334 ± 0.0187	0.209 ± 0.0428
2.100	0.039	92.280	81.12° - 81.23°	0.197	0.121 ± 0.0370
(H) Tundra – no snow (June 12, 1995)					
0.472	0.021	1962.9	82.00° - 82.61°	0.053 ± 0.0026	0.027 ± 0.0231
0.675	0.020	1471.7	82.00° - 82.61°	0.096 ± 0.0016	0.056 ± 0.0292
0.869	0.020	943.60	82.00° - 82.61°	0.260 ± 0.0007	0.179 ± 0.0378
1.038	0.020	671.13	82.00° - 82.61°	0.331 ± 0.0015	0.231 ± 0.0479
1.219	0.021	475.07	82.00° - 82.61°	0.298 ± 0.0025	0.211 ± 0.0420
1.271	0.020	430.81	82.00° - 82.61°	0.244 ± 0.0008	0.176 ± 0.0367
1.643	0.041	229.64	82.00° - 82.26°	0.328 ± 0.0054	0.241 ± 0.0412
2.100	0.039	92.280	82.38° - 82.61°	0.191 ± 0.0002	0.128 ± 0.0461

* Albedo is defined in section 2 (eqn. 3) as the ratio of the ratio of the upward flux to the downward flux at the top of the atmosphere. The Albedo values at 0.47 and 0.50 μm and to a lesser extent, the 0.67 μm are significantly reduced by Rayleigh scattering.

FIGURE LEGENDS

Figure 1. Approximate location of each set of sea ice and tundra BRF measurements.

Figure 2. Sample photos of each of the four surface types measured: (a) snow-covered sea ice; (b) melt-season sea ice; (c) snow-covered tundra (Trans-Alaska Pipeline and road in upper right corner of photo); and (d) tundra shortly after snow melt. Photos a-c were taken from the University of Washington C-131A aircraft, whereas photo d was taken from the ground. Photos by Michael D. King.

Figure 3. Spectral measurements of surface-atmosphere bidirectional reflectance over snow-covered sea ice on April 7, 1992 during LEADEX. All bands are from BRF A (see figure 1) except i (2.2 μm) which is from BRF B. The location of the anti-solar point at $\theta = 65°$ and $\phi = 180°$ is indicated in figure 3a.

Figure 4. Representative angular distribution of BRF in the principal plane for (a) the snow-covered and (b) melt-season sea ice surfaces. The capital letter after each channel label denotes from which BRF the principal plane plot was derived.

Figure 5. Spectral measurements of surface-atmosphere bidirectional reflectance over melt-season sea ice. This case is BRF D from June 8, 1995 during ARMCAS, but is representative of the other two melt-season sea ice cases. The location of the anti-solar point at $\theta = 55°$ and $\phi = 180°$ is indicated in figure 5a.

Figure 6. Spectral measurements of surface-atmosphere bidirectional reflectance over snow-covered tundra. This case is from BRF F from April 7, 1992 during LEADEX. The location of the anti-solar point at $\theta = 65°$ and $\phi =$

180° is indicated in figure 6a.

Figure 7. Representative angular distribution of BRF in the principal plane for the (a) snow-covered and (b) snow-free tundra surfaces. The capital letter after each channel label denotes from which BRF the principal plane plot was derived.

Figure 8. Spectral measurements of surface-atmosphere bidirectional reflectance over snow- free tundra. This case is BRF G on June 12, 1995 during ARMCAS. The location of the anti-solar point at $\theta = 81°$ and $\phi = 180°$ is indicated in figure 8a.

Figure 9. Figure 9. Ratio of nadir reflectance to hemispherical albedo plotted as a function of wavelength for BRFs A-H.

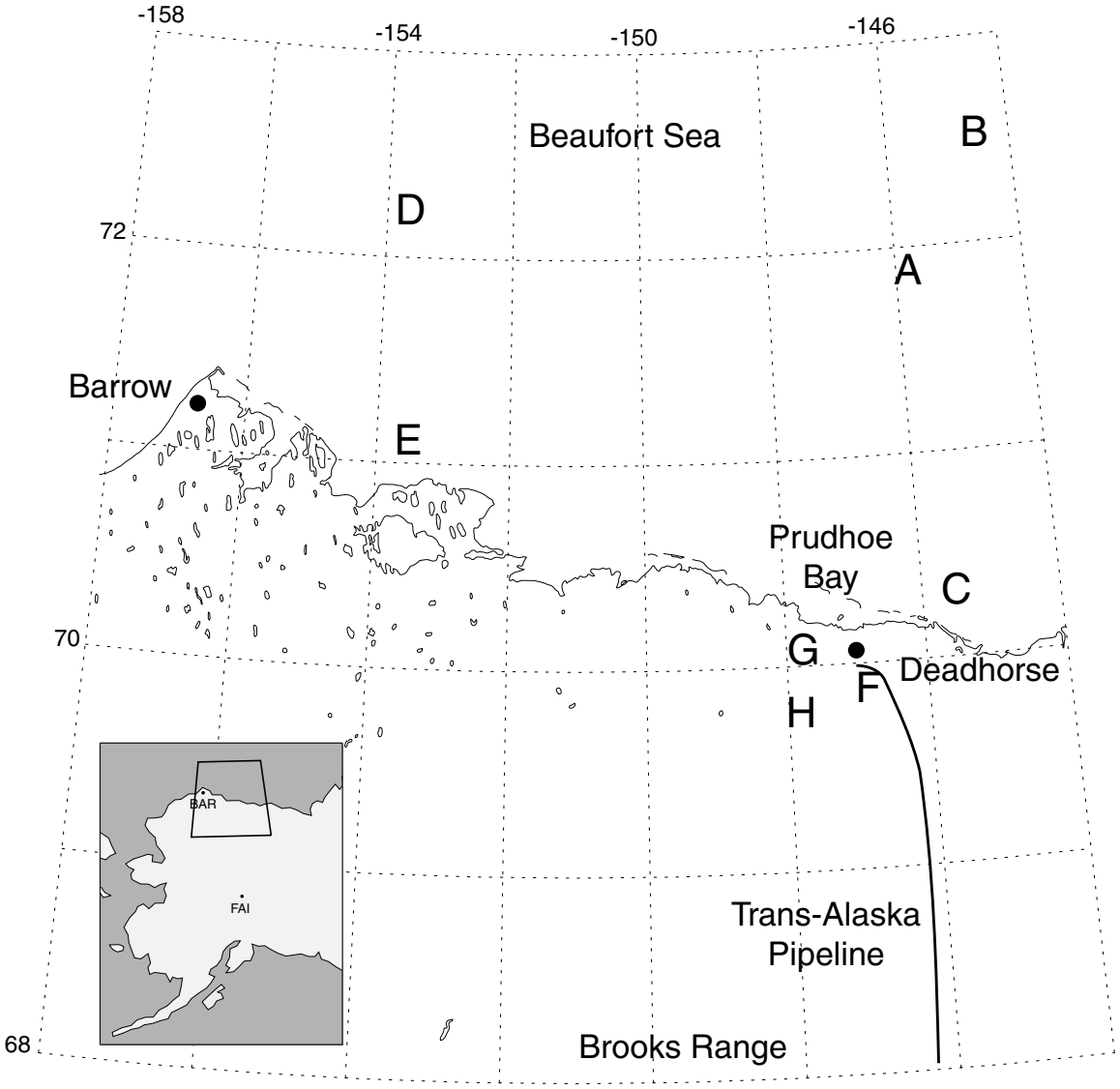

Sea Ice	Tundra
A - Apr. 7, 1992	F - Apr. 7, 1992
B - Apr. 7, 1992	G - Jun. 12, 1995
C - Jun. 5, 1995	H - Jun. 12, 1995
D - Jun. 8, 1995	
E - Jun. 8, 1995	

Figure 1. Approximate location of each set of sea ice and tundra BRF measurements.

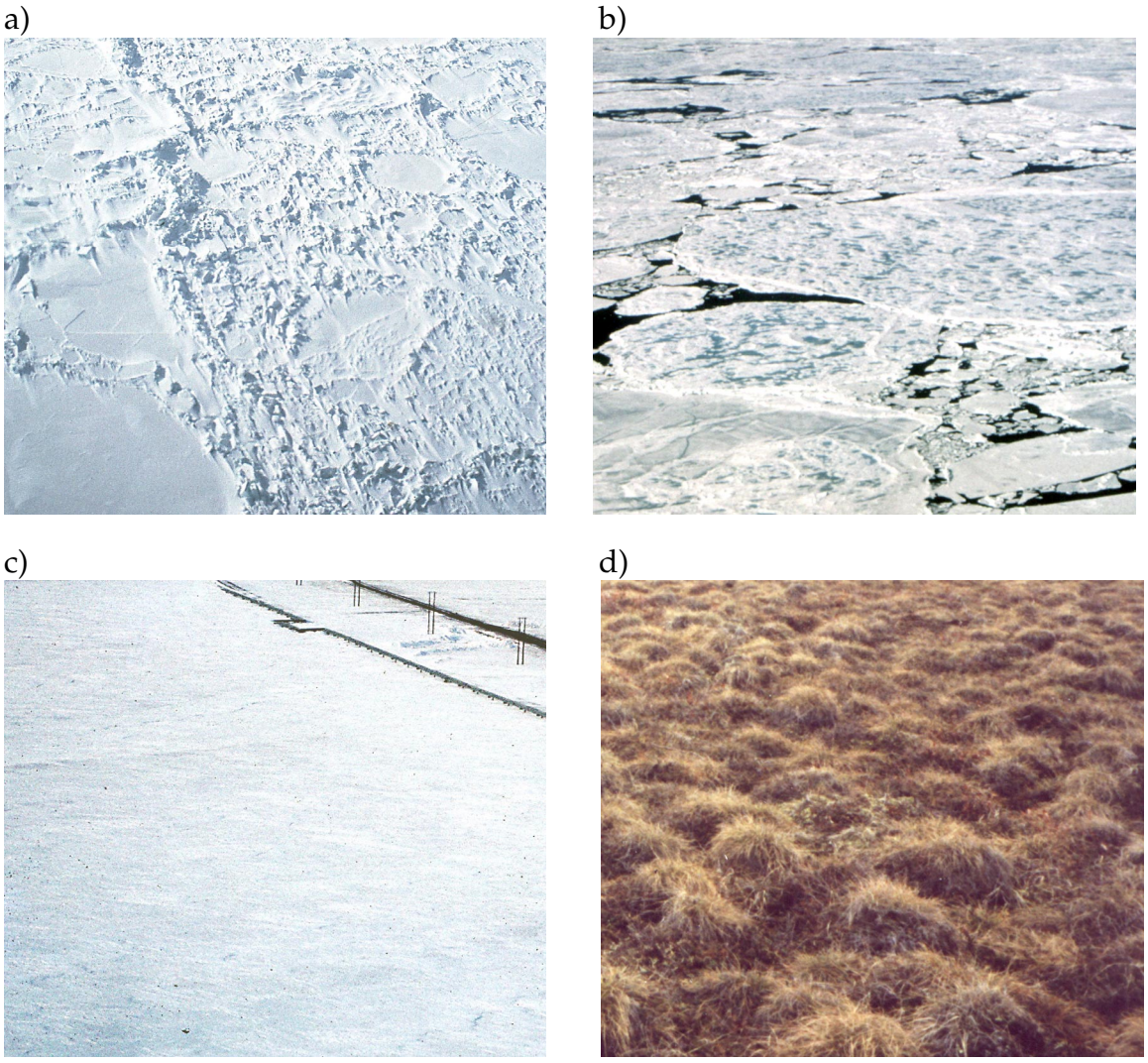

Figure 2. Sample photos of each of the four surface types measured: (a) snow-covered sea ice; (b) melt-season sea ice; (c) snow-covered tundra (Trans-Alaska Pipeline and road in upper right corner of photo); and (d) tundra shortly after snow melt. Photos a-c were taken from the University of Washington C-131A aircraft, whereas photo d was taken from the ground. Photos by Michael D. King.

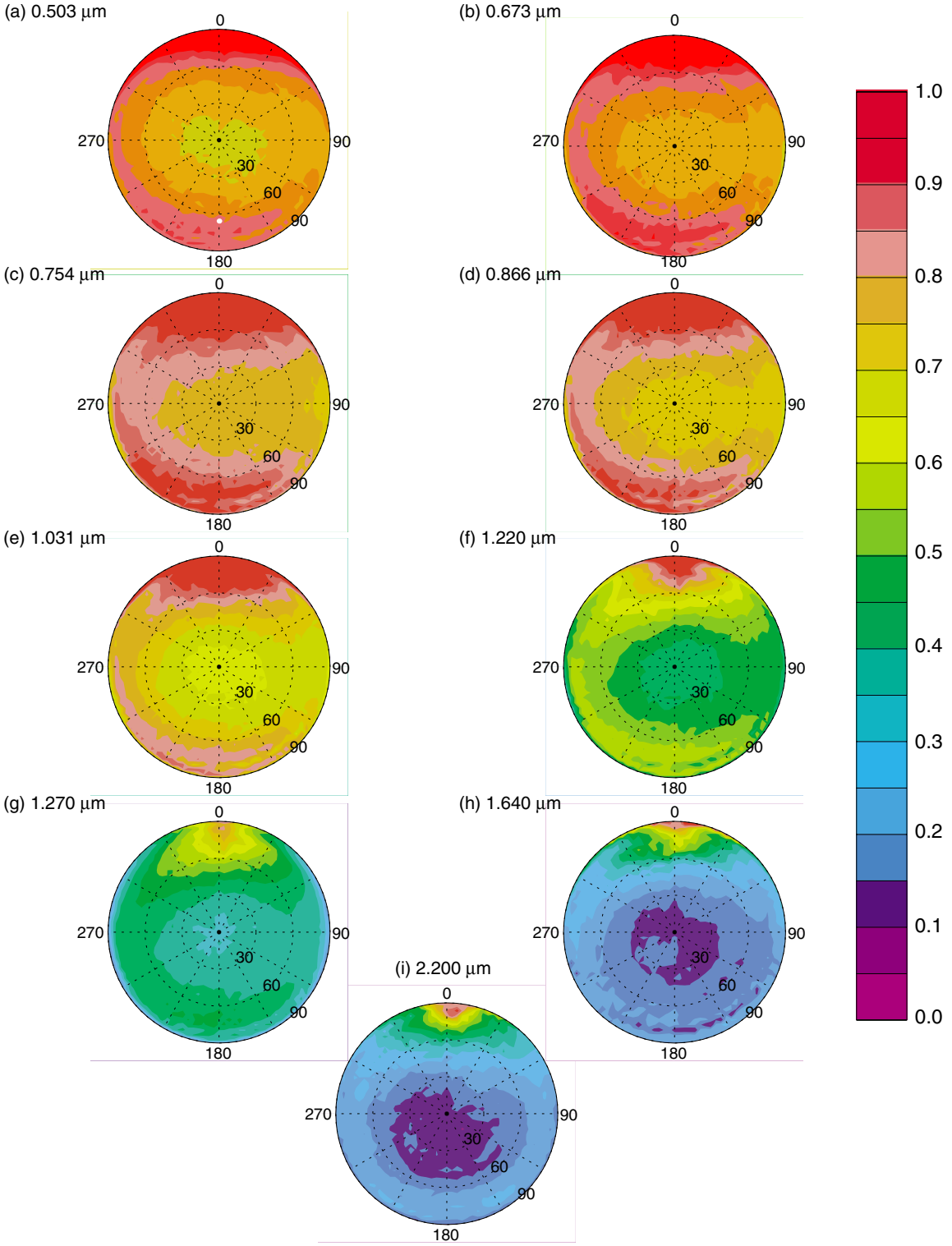

Figure 3. Spectral measurements of surface-atmosphere bidirectional reflectance over snow-covered sea ice on April 7, 1992 during LEADEX. All bands are from BRF A (see figure 1) except i (2.2 µm) which is from BRF B. The location of the anti-solar point at $\theta = 65°$ and $\phi = 180°$ is indicated in figure 3a.

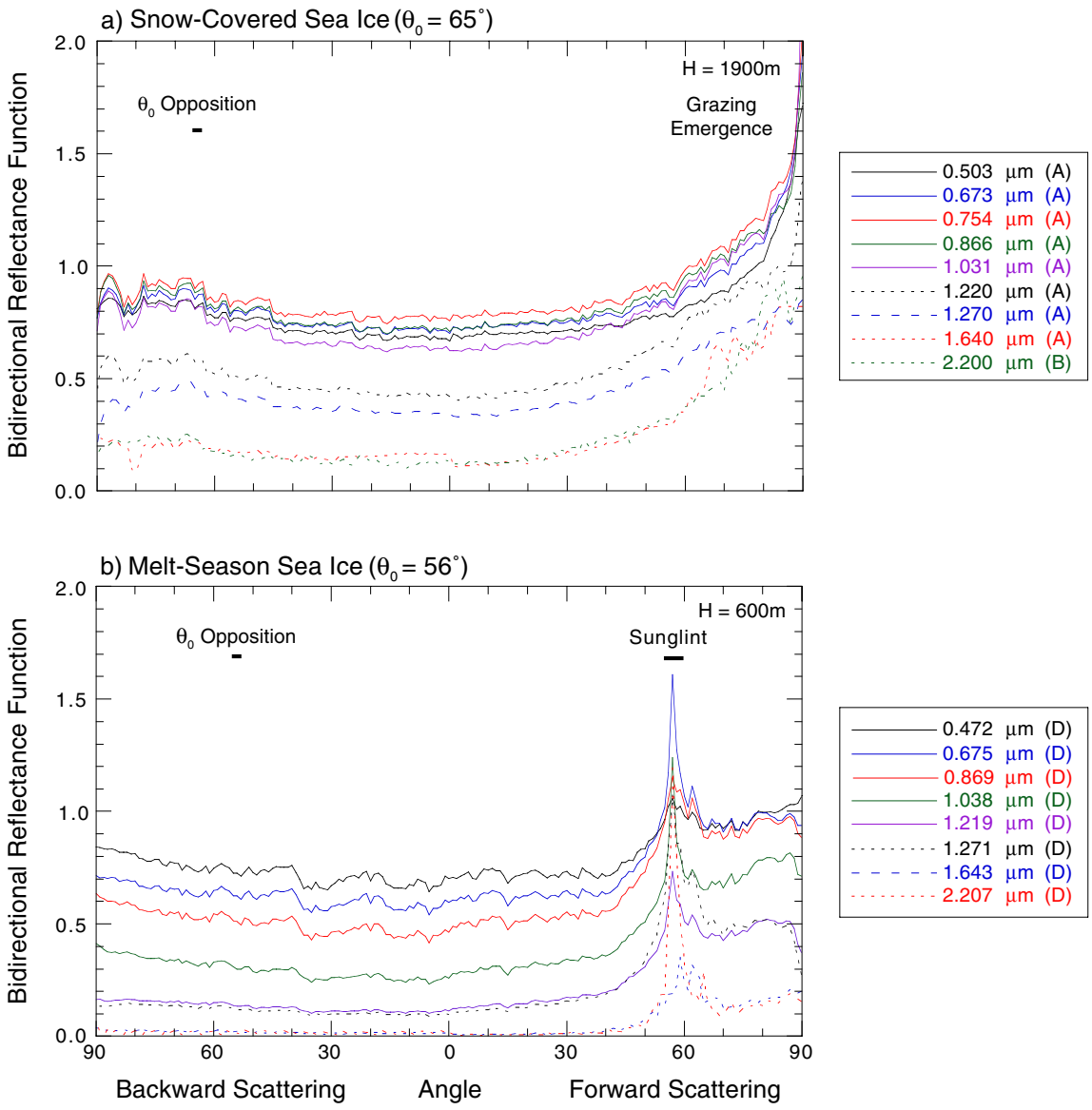

Figure 4. Representative angular distribution of BRF in the principal plane for (a) the snow-covered and (b) melt-season sea ice surfaces. The capital letter after each channel label denotes from which BRF the principal plane plot was derived.

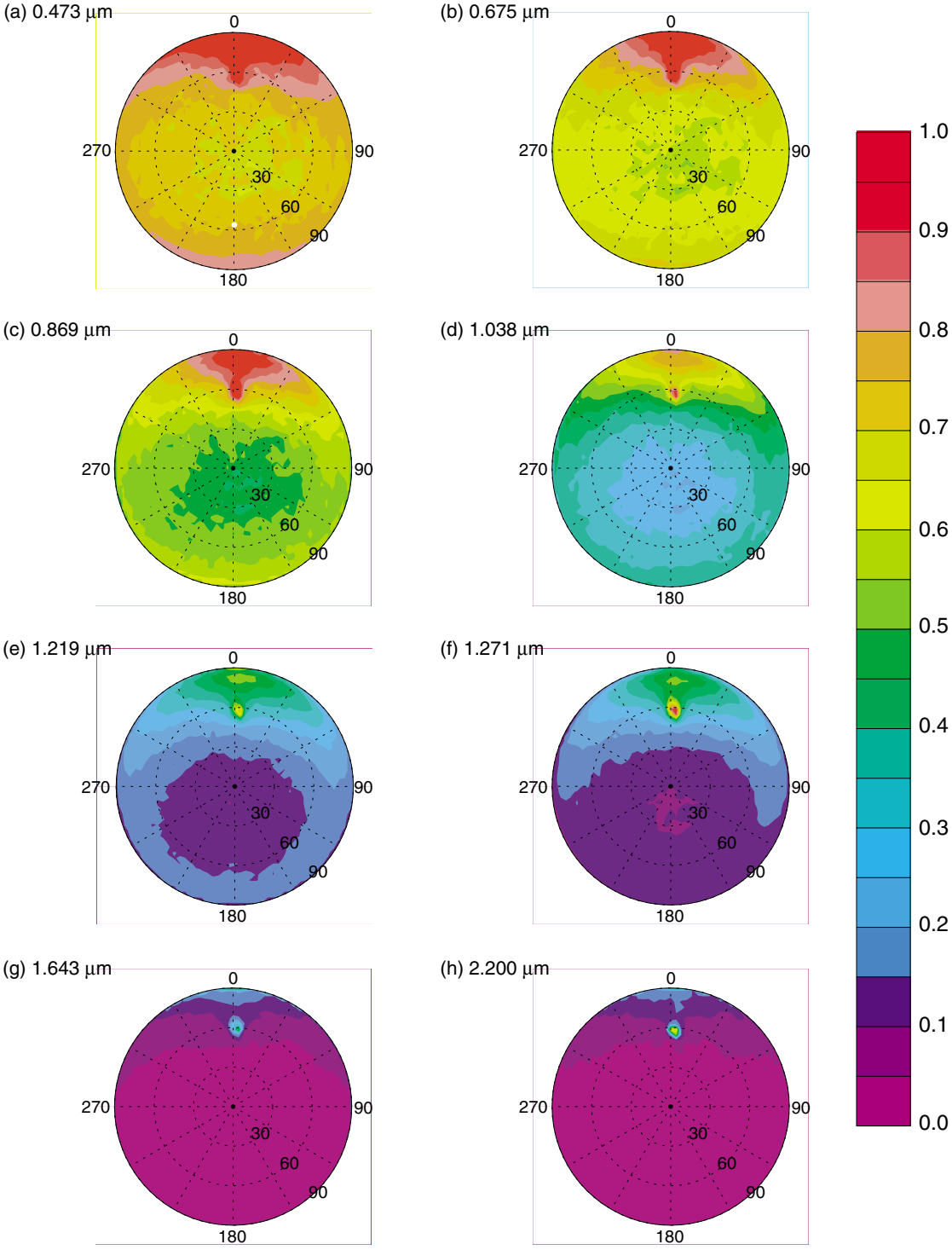

Figure 5. Spectral measurements of surface-atmosphere bidirectional reflectance over melt-season sea ice. This case is BRF D from June 8, 1995 during ARMCAS, but is representative of the other two melt-season sea ice cases. The location of the anti-solar point at $\theta = 55°$ and $\phi = 180°$ is indicated in figure 5a.

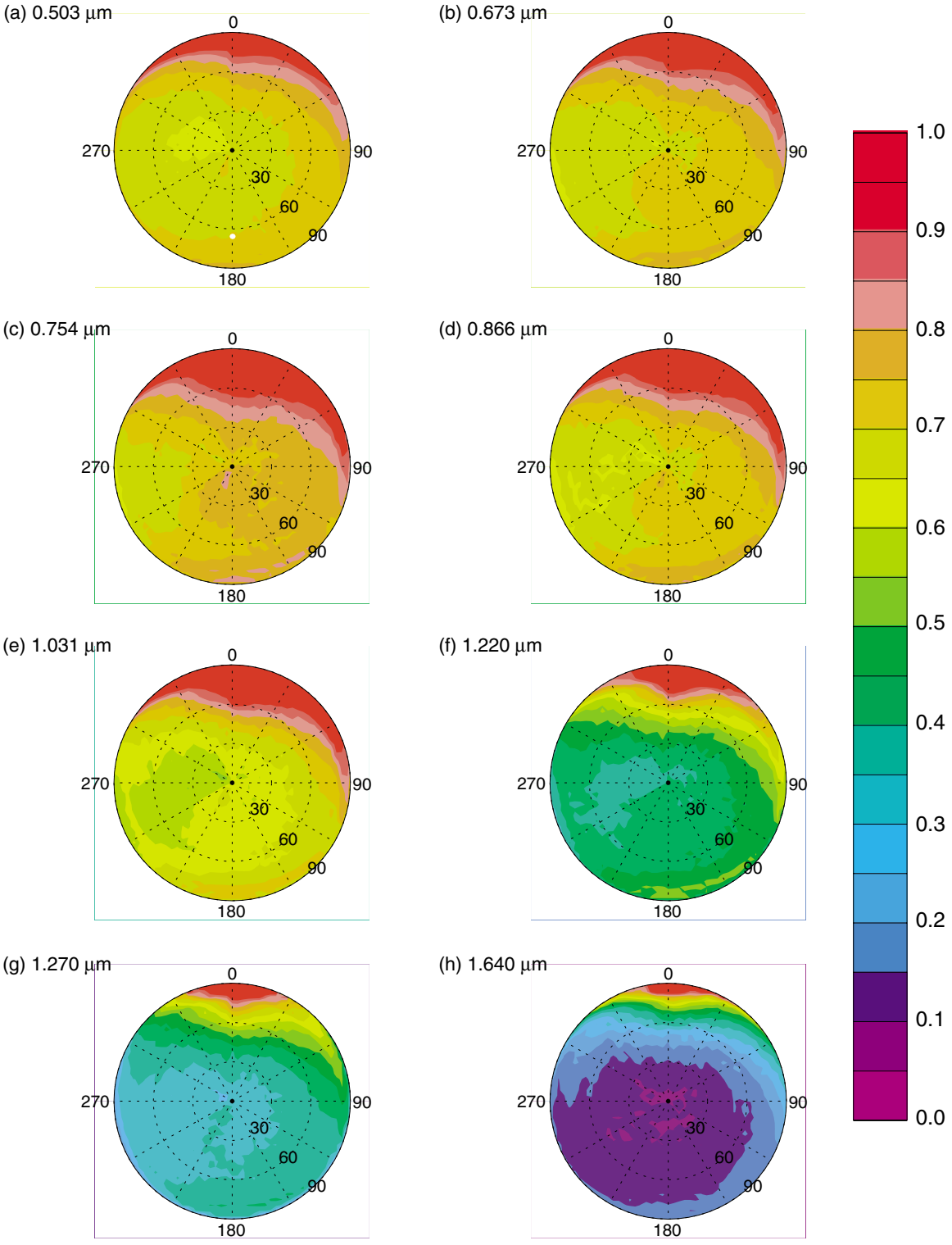

Figure 6. Spectral measurements of surface-atmosphere bidirectional reflectance over snow-covered tundra. This case is from BRF F from April 7, 1992 during LEADEX. The location of the anti-solar point at $\theta = 65°$ and $\phi = 180°$ is indicated in figure 6a.

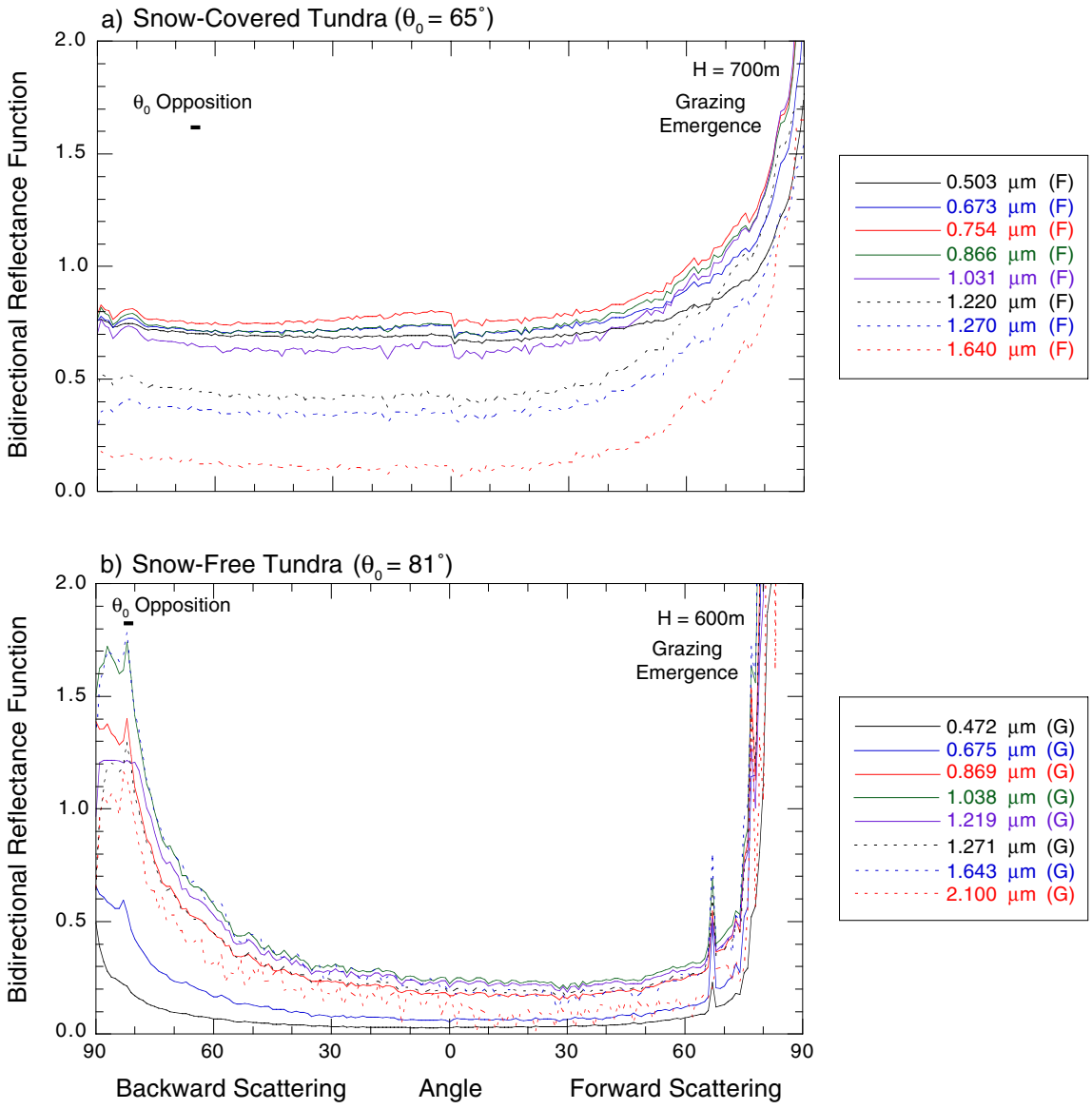

Figure 7. Representative angular distribution of BRF in the principal plane for the (a) snow-covered and (b) snow-free tundra surfaces. The capital letter after each channel label denotes from which BRF the principal plane plot was derived.

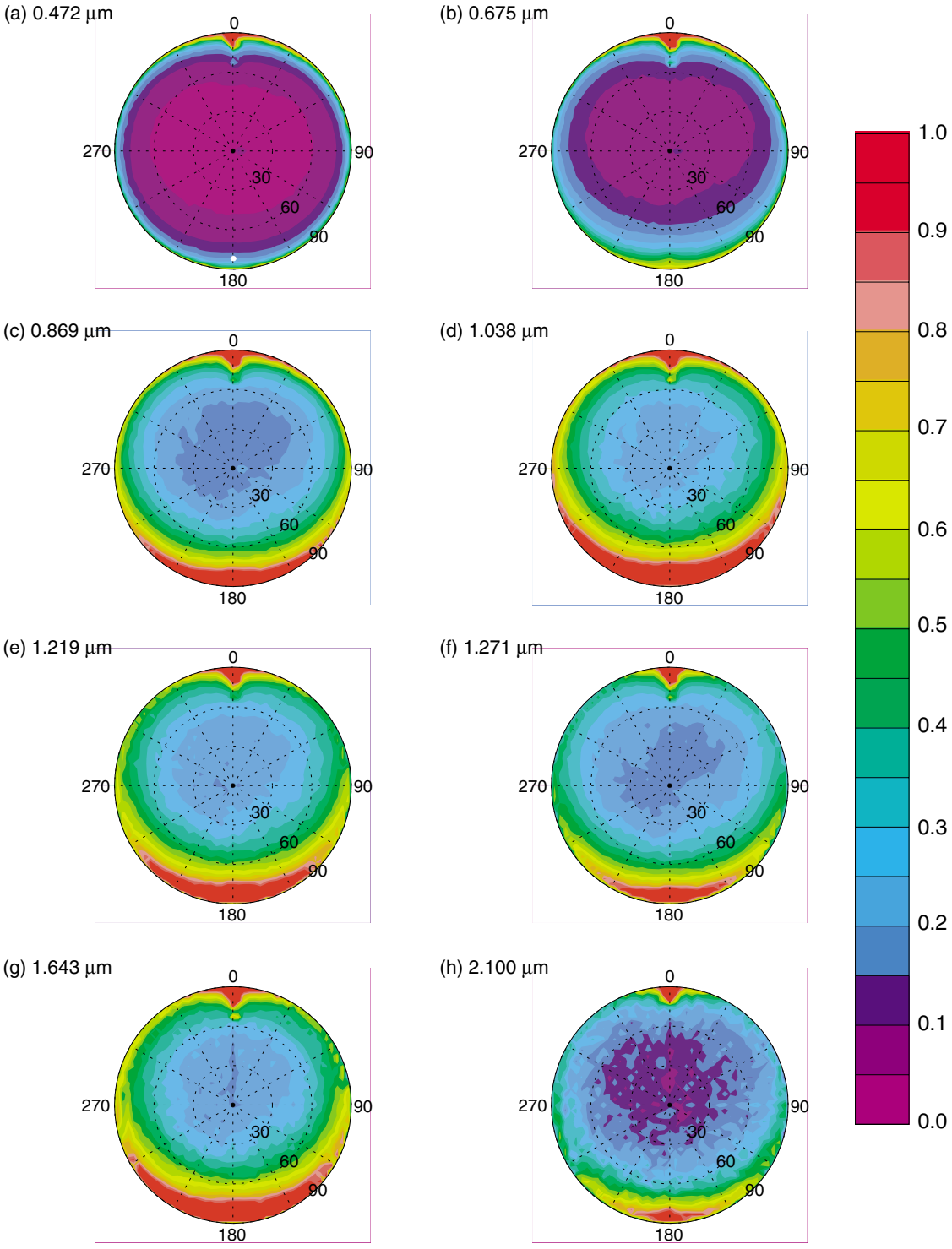

Figure 8. Spectral measurements of surface-atmosphere bidirectional reflectance over snow- free tundra. This case is BRF G on June 12, 1995 during ARMCAS. The location of the anti-solar point at $\theta = 81°$ and $\phi = 180°$ is indicated in figure 8a.

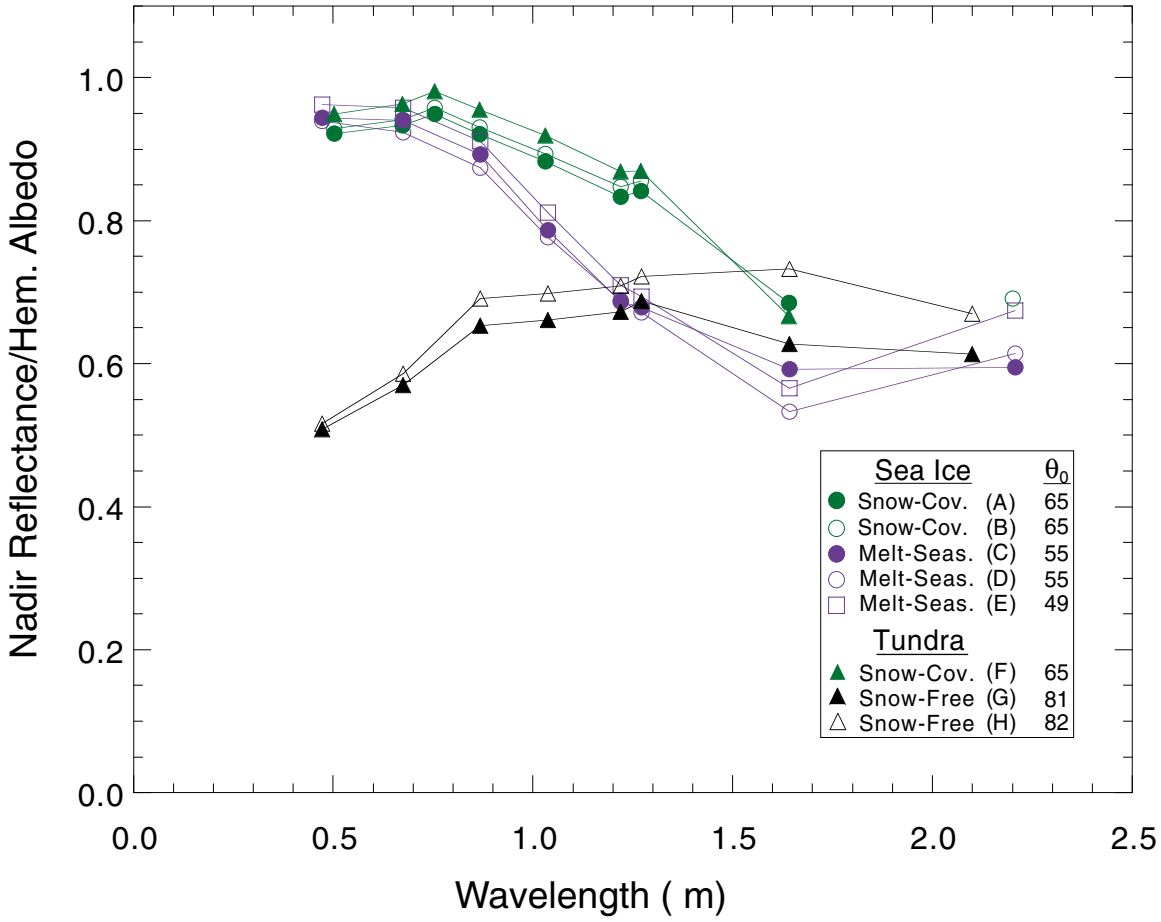

Figure 9. Ratio of nadir reflectance to hemispherical albedo plotted as a function of wavelength for BRFs A-H.